

# The far-infrared signature of dust in high-latitude regions

C. del Burgo,<sup>1,2★</sup> R. J. Laureijs,<sup>1,3</sup> P. Ábrahám<sup>2,4</sup> and Cs. Kiss<sup>4</sup>

<sup>1</sup>European Space & Technology Centre (ESTEC), Keplerlaan 1, Postbus 299, 2200 AG Noordwijk, the Netherlands

<sup>2</sup>Max-Planck-Institut für Astronomie, Königstuhl 17, D-69117 Heidelberg, Germany

<sup>3</sup>ISO Data Centre, Astrophysics Division of ESA, Villafranca del Castillo, PO Box 50727, E-28080 Madrid, Spain

<sup>4</sup>Konkoly Observatory of the Hungarian Academy of Sciences, PO Box 67, H-1525 Budapest, Hungary

Accepted 2003 August 4. Received 2003 July 18; in original form 2003 March 21

## ABSTRACT

We present ISOPHOT observations of eight interstellar regions in the 60–200  $\mu\text{m}$  wavelength range. The regions belong to mostly quiescent high-latitude clouds and have optical extinction peaks from  $A_V \sim 1$ –6 mag. From the 150- and 200- $\mu\text{m}$  emission, we derived colour temperatures for the classical big grain component which show a clear trend of decreasing temperature with increasing 200- $\mu\text{m}$  emission. The 200- $\mu\text{m}$  emission per unit  $A_V$ , however, does not drop at lower temperatures. This fact can be interpreted in terms of an increased far-infrared (FIR) emissivity of the big grains. We developed a two-component model including warm dust with the temperature of the diffuse interstellar medium (ISM) of  $T = 17.5$  K, and cold dust with  $T = 13.5$  K and FIR emissivity increased by a factor of  $>4$ . A mixture of the two components can reproduce the observed colour variations and the ratios  $I_{200}/A_V$  and  $\tau_{200}/A_V$ . The relative abundance of small grains with respect to the big grains shows significant variations from region to region at low column densities. However, in lines of sight of higher column density, our data indicate the disappearance of small grains, perhaps a signature of adsorption/coagulation of dust. The larger size and porous structure could also explain the increased FIR emissivity. Our results from eight independent regions suggest that these grains might be ubiquitous in the galactic ISM.

**Key words:** ISM: clouds – dust, extinction – infrared: ISM.

## 1 INTRODUCTION

Infrared colour variations measured in interstellar cirrus and molecular clouds have proven to be powerful indicators of not only variations due to radiative transfer (Laureijs, Mattila & Schnur 1987; Bernard et al. 1992), but also of variations in the relative abundances between different dust components emitting in the infrared (Boulanger et al. 1990). The mid- and far-infrared (FIR) emission of diffuse interstellar dust is usually interpreted in terms of a three-component dust model – polycyclic aromatic hydrocarbons (PAHs), very small grains and big grains – deduced from *IRAS* observations (e.g. Desert, Boulanger & Puget 1990).

The study by Boulanger et al. (1990) showed that the abundance of the PAH dust component emitting in the 5–15  $\mu\text{m}$  range varies with respect to the big grain component emitting at 100  $\mu\text{m}$ . Similarly, Lagache et al. (1998) found that also the abundance of the small grain component, mainly responsible for the emission around 60  $\mu\text{m}$ , can vary relative to the big grain component.

The submillimetre balloon experiment *PRONAOS* observed regions where the *IRAS* 60- $\mu\text{m}$  component appears to be absent

(Bernard et al. 1999; Stepnik et al. 2003). *PRONAOS* showed that the temperature of the big dust grains in those regions is too low (12 K assuming a  $\nu^{-2}$  emissivity law) for particles with properties derived from the diffuse interstellar medium (DISM). This suggests that big grains in 60- $\mu\text{m}$  emission-deficient regions are significantly different from those in the DISM. The big grains have probably changed their properties due to adsorption/coagulation of small dust grains on to big grains. These studies support the view that abundance variations among the different dust components in the interstellar medium (ISM) cannot be independent due to the physical interaction of the components inside the clouds.

In this paper we study the FIR colours of eight mostly quiescent high-latitude dust regions in the 60–200  $\mu\text{m}$  wavelength range observed with the ISOPHOT instrument (Lemke et al. 1996) on board the European Space Agency (ESA) *Infrared Space Observatory* (*ISO*; Kessler et al. 1996). Most of the dust regions were selected from *IRAS* images because they include dense zones with regular infrared morphology and well-defined cold cores. To estimate the dust column density independently from the infrared emission we have obtained extinction maps from star counts using the United States Naval Observatory (USNO) Catalogue. The combination of the FIR and extinction data sets provides information on several

★E-mail: cburgo@rssd.esa.int (CdB)

**Table 1.** ISOPHOT observations.

Region	$\alpha_{J2000}$ (hh mm ss)	$\delta_{J2000}$ (dd mm ss)	<i>ISO</i> <sub>id</sub>	$\lambda_{\text{ref}}$ ( $\mu\text{m}$ )	Area (arcmin <sup>2</sup> )	Remark
G6.5+36.5	15 56 0.7	−2 44 21.2	10101301	60, 90	185.2	Part of L183E
			10101302	150, 200	206.9	
G89.0−41.2	23 08 35.2	14 46 3.4	21600513	60, 90	51.7	Part of MBM55
			21600514	150, 200	206.9	
G90.7+38.0	16 50 53.3	60 55 37.2	27701702	60, 100	112.9	Part of Draco
			27701701	150, 200	183.4	
G111.2+19.6	21 02 16.8	76 51 45.1	11101606	150, 200	249.2	Part of L1228
G187.4−16.7	5 02 24.3	13 40 58.8	82901030	60, 90	174.6	Part of L1563,
			82900834	80	97.0	In Taurus
			86501535	100	97.0	
			82901031	120, 200	253.9	
G297.3−15.7	11 08 6.5	−77 28 53.5	26101501	150	1469.4	Part of Chamaeleon I
			26101401	200	1469.4	
G301.2−16.5	12 16 22.5	−79 17 8.9	60601026	60, 90	99.3	In the border of Chamaeleon III
			60601027	120, 150, 200	115.2	
G301.7−16.6	12 25 23.8	−79 22 47.6	60600924	60, 90	169.9	In the border of Chamaeleon III
			60600925	120, 150, 200	115.2	

aspects of the infrared signature of dust grains: (1) the variation of the temperature of the big grains inside the clouds' regions and among the regions in the sample; (2) the behaviour of the emission of the small grains with respect to the big grain emission; and (3) the determination of the dust emission per unit extinction at FIR wavelengths. The present data are also useful to investigate whether the processes observed by *PRONAOS* are the exceptions or the rule in the ISM. In Section 2 we present our sample of eight high-latitude interstellar regions. Section 3 is devoted to the data processing. The results are included in Section 4, and the interpretation in Section 5. Finally, Sections 6 and 7 present the discussion and the conclusions, respectively.

## 2 PRESENTATION OF THE SAMPLE

The sample comprises eight nearby interstellar regions, including a faint region located in Draco and a bright region in Chamaeleon (a low mass star forming nebula). All regions are situated at Galactic latitudes  $|b| > 15^\circ$  and are parts of clouds. They present peak column densities from diffuse to moderately dense ISM with  $A_V$  ranging from 0.2 to 6 mag, and do not always cover the densest part or brightness peak of the cloud or nebula.

The observations were retrieved from the *ISO* Archive (Kessler et al. 2000). For each region at least two different FIR wavelengths were observed, including a measurement at 200  $\mu\text{m}$  to gauge the emission of the big grains.

Table 1 summarizes the ISOPHOT observations. The table contains the region's name deduced from the galactic coordinates, the *ISO* identification number (*ISO*<sub>id</sub>) as given in the *ISO* Data Archive,<sup>1</sup> the reference wavelengths of the ISOPHOT filter bands ( $\lambda_{\text{ref}}$ ), the size of the area sampled and the name of the cloud associated with the region.

## 3 DATA PROCESSING

### 3.1 ISOPHOT observations

The regions were mapped with ISOPHOT using the Astronomical Observation Template PHT22 in raster mapping mode with array

detectors C100 ( $3 \times 3$  pixels; 46 arcsec pixel<sup>−1</sup>) and C200 ( $2 \times 2$  pixel; 92 arcsec pixel<sup>−1</sup>). For an overview see the ISOPHOT Handbook (Laureijs et al. 2003).

Each map was bracketed with two measurements of the internal fine calibration source (FCS) obtained with the same filter as the map. The observations at 120, 150 and 200  $\mu\text{m}$  form a homogeneous data set, all corresponding to the same detector (C200) and to the same aperture. Similarly, the surface brightness measurements at 60, 80, 90 and 100  $\mu\text{m}$  were all performed with the C100 detector and the 46-arcsec aperture.

The data were processed using the ISOPHOT Interactive Analysis software PIA V9.1 (Gabriel et al. 1997). After correcting for cosmic glitches, signals corresponding to the same sky position were averaged. Signal transients, the slow response of the ISOPHOT detectors for flux changes, were visible only on the first few raster steps of our observations, but they did not affect the main bodies of the maps due to the long exposure times of the rasters. Because the sampled areas do not contain strong compact sources, memory effects due to crossing bright sources were negligible. All standard signal correction steps (reset interval correction, dark subtraction, signal linearization) were applied. For flux calibration the detector's actual responsivity was derived from the second FCS measurement, obtained just after the map. For G90.7+38.0, the faint region in Draco, it was not possible to obtain the actual responsivity of the C200 detector because the heating power of the FCS was below its calibrated range. Instead, the default responsivities were used to calibrate in flux. Unless explicitly stated no colour correction was applied on the data.

We used the first quartile normalization flat-fielding method as implemented in PIA in order to correct for the remaining responsivity differences of the individual detector pixels. Maps obtained with the C100 detector had intrinsically higher spatial resolution than the rasters obtained with C200. For the homogeneity of the data base, however, we created C100 maps with the spatial resolution and grid matching those of the C200 rasters, by (1) convolution of the original C100 image with the theoretical C200 beam profile, and (2) resampling according to the pixel size and grid of C200 image.

As an example of the data quality, Fig. 1 shows the maps at 90, 120 and 200  $\mu\text{m}$  for the region G187.4−16.7 (in L1563). The convolved 90- $\mu\text{m}$  map is also shown to illustrate the beam size correction and

<sup>1</sup> Available at <http://www.iso.vilspa.esa.es/ida/>

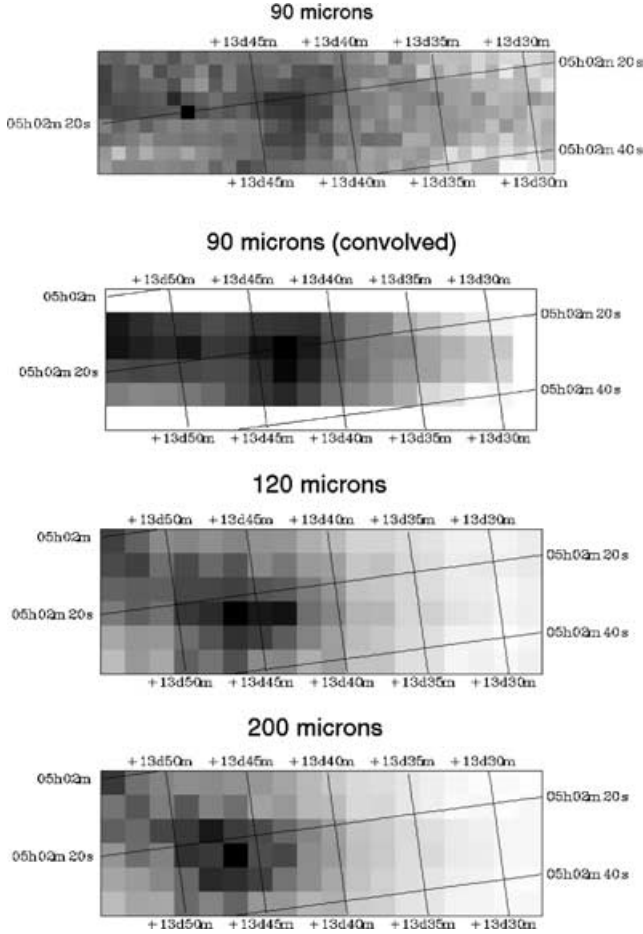


**Figure 1.** From top to bottom: surface brightness ( $I_\nu$ ) maps of G187.4–16.7 (region in L1563) at 90, 120 and 200  $\mu\text{m}$ .  $I_\nu$  ranges are 17–27  $\text{MJy sr}^{-1}$  (90  $\mu\text{m}$ ), 19–24  $\text{MJy sr}^{-1}$  (90  $\mu\text{m}$  convolved image), 23–57  $\text{MJy sr}^{-1}$  (120  $\mu\text{m}$ ), and 31–99  $\text{MJy sr}^{-1}$  (200  $\mu\text{m}$ ). ZL emission was not subtracted. Darker regions are brighter. See Fig. 2 for absolute scale.

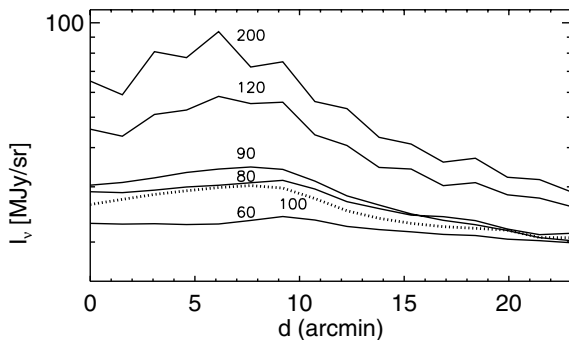


**Figure 2.** A scan over the region G187.4–16.7 for all wavelengths observed with ISOPHOT ( $\lambda_{\text{ref}} = 60, 80, 90, 100, 120$  and  $200 \mu\text{m}$ ). The scan covers a width of 1.5 arcmin starting at position  $\alpha_{J2000} = 5^{\text{h}}2^{\text{m}}21^{\text{s}}.4$ ,  $\delta_{J2000} = 13^{\circ}52'32''$  and ending at position  $\alpha_{J2000} = 5^{\text{h}}2^{\text{m}}33^{\text{s}}.9$ ,  $\delta_{J2000} = 13^{\circ}29'38''$ . Each surface brightness  $I_\nu$  was smoothed to the resolution of the 200- $\mu\text{m}$  scan. ZL emission was not subtracted.

resampling methods. In Fig. 2 the surface brightness  $I_\nu$  is plotted for the same region along a scan at different ISOPHOT filter bands ( $\lambda_{\text{ref}} = 60, 80, 90, 100, 120$  and  $200 \mu\text{m}$ ). Note that the position of the surface brightness peak at shorter wavelengths (60 and 80  $\mu\text{m}$ ) differs from the FIR peak by about 2 arcmin.

The absolute calibration accuracy of the surface brightness values in the maps is estimated to be around 20–30 per cent, depending on the brightness level. This amount includes both statistical uncertainties (also known as random errors) due to the signal derivation process and systematic uncertainties related to the different calibration steps. The random error components come from readout noise, uncorrected cosmic glitches and signal transients. The variation of the actual responsivity with time, a characteristic of the Ge:Ga FIR detectors of ISOPHOT, was monitored by evaluating the FCS measurements related to each map. These calibration observations have their own uncertainties which also contribute to the total error budget. The systematic uncertainties include the following factors: (1) formal error bars of the coefficients of the standard calibration steps, such as reset interval correction, dark subtraction, signal linearization (fortunately, the signals from the internal calibration source were successfully matched to the observed sky brightness, thus the detector non-linearity problems were mainly cancelled); (2) uncertainty in the flux calibration of the internal calibration source (FCS); (3) uncertainty in the absolute photometric zero-point of the ISOPHOT FIR detectors; (4) any possible uncertainty related to the filter transmission curves and to the effective solid angle values of the detector pixels per filter. However, in Section 4.1 we show that most of these error components are cancelled when considering colours instead of absolute fluxes. Therefore, the uncertainties corresponding to our FIR colour measurements are significantly lower than the 20–30 per cent quoted for the absolute brightness values.

### 3.2 Extinction maps

Extinction maps for the sample of dust regions (see Table 1) were obtained in two different ways. In the first approach, we used a star count method applied to an optical image. Using the electronic version of the USNO A2.0 Catalogue,<sup>2</sup> we extracted coordinates and  $B$  (blue) magnitudes for stars in the areas corresponding to the ISOPHOT 200- $\mu\text{m}$  maps. For each dust region an area close to the target for the definition of the reference star counts was also included. In these regions no obvious extinction feature was visible in the Digitized Sky Survey (DSS)<sup>3</sup> image. A cumulative star count ( $\log(N)$ ) versus  $B$ -magnitude diagram was constructed for each region. We selected only the linear part of the diagram, i.e. stars brighter than  $B = 18$  mag (the completeness limit of the catalogue). Stars fainter than this limiting magnitude are not reliable. In this way, we eliminated spurious sources and other artefacts. Parameters of this curve were used to obtain the  $B$  extinction values. A detailed description of the method can be found in Bok (1956) and Dickman (1978). The spatial resolution of the extinction maps was chosen to be 3 arcmin. When comparing FIR and extinction data, ISOPHOT surface brightness maps were smoothed to the 3-arcmin resolution of the extinction maps. The extinction data  $A_B$  were transformed to  $A_V$  assuming a total-to-selective extinction ratio of  $R_V = 3.1$ . This value of  $R_V$  is the averaged value in the DISM (Mathis 1990). A higher value of  $R_V = 5.0$ , which is observed in molecular clouds, but not systematically, would increase our extinction values by 10 per cent.

In the second approach we derived extinction maps by using the Two Micron All Sky Survey (2MASS)  $JHK$  photometry as described in Lombardi & Alves (1996). These data could have been better suited for our purposes because the extinction data do not depend

<sup>2</sup> Available at <http://www.nofs.navy.mil>

<sup>3</sup> Available at <http://archive.eso.org/dss/dss>

on the value of the total-to-selective absorption index. However, the resulting maps, and later the  $I_{200}$  versus  $A_V$  correlation diagrams (Section 4.1), turned out to be systematically noisier than the maps based on the USNO Catalogue, thus we decided to use the results of the first approach in the further analyses.

### 3.3 COBE/DIRBE data

When absolute intensities rather than colours were investigated, we subtracted the zodiacal light (ZL). We made a prediction of the zodiacal sky brightness for each ISOPHOT observation using the *Cosmic Background Explorer*/Diffuse Infrared Background Experiment (COBE/DIRBE) Sky and Zodi Atlas (Kelsall et al. 1998). First, the surface brightness values in the 10 DIRBE photometric bands were extracted for the positions and dates of the ISOPHOT observations. Secondly, the spectral energy distributions defined by the 10 photometric values were convolved with the DIRBE filter profiles to compute colour correction factors. Thirdly, an interpolation was performed among the colour corrected DIRBE flux densities at the ISOPHOT reference wavelengths. Finally, the predicted flux values were derived by applying an ‘inverse colour correction’ using the respective ISOPHOT colour correction factors. These flux values can be subtracted from the ISOPHOT measurements. We made no attempt to correct for possible systematic difference between the DIRBE and the ISOPHOT photometric systems. Because the ZL is almost constant over the scales of our scans/maps, the same predicted value was subtracted from the entire area sampled in each raster. Table 2 lists the ZL values associated with each region for the ISOPHOT filter bands.

We also determined the DIRBE surface brightness corresponding to the cirrus emission. We used the DIRBE ZL Subtracted Mission Averaged (ZSMA) maps<sup>4</sup> for the cirrus component. The 10-band DIRBE photometric values for a given position were extracted. We computed the median of all DIRBE pixels within a radius of 0.4 deg (4–5 DIRBE pixels). A modified blackbody function with a dust emissivity coefficient  $\beta = 2$  was fitted to the 100- and 240- $\mu\text{m}$  cirrus surface brightness. As for determining the ZL we transformed these DIRBE brightnesses to the ISOPHOT filter bands. In addition, a sky background position associated with each region (distance  $< 2^\circ$ ) was selected and its predicted DIRBE surface brightness computed. Predicted DIRBE values for the local sky background (LSB) and the surface brightness of the regions are compiled in Tables 2 and 3, respectively.

## 4 RESULTS

### 4.1 Far-infrared colours

An overview of the infrared emission for all regions in the sample is presented in Fig. 3. The emission for each 200- $\mu\text{m}$  position is correlated with the emission in the other filter bands after beam size correction and grid transformation (see Section 3.1). Any colour variation will result in a deviation from linearity in the correlation. In the remainder of this paper, the surface brightness emission  $I_\nu$  (in  $\text{MJy sr}^{-1}$ ) in the 60-, 90-, 150- and 200- $\mu\text{m}$  ISOPHOT bands is written as  $I_{60}$ ,  $I_{90}$ ,  $I_{150}$  and  $I_{200}$ , respectively.

For each region, the  $I_{150}$ – $I_{200}$  correlation is linear within the scatter and no significant change in the slope is observed. Note that

these regions cover different 200- $\mu\text{m}$  emission ranges (see Fig. 3). We verified the linearity by fitting a second-order polynomial to the correlation  $I_{150}$  versus  $I_{200}$ . The coefficient related to the quadratic term turned out to be in all cases insignificant, less than  $1\sigma$ . Local deviations from the mean correlation can occur, but these will affect a few points in the diagram corresponding to only a small area of the sky. Hereafter we refer to the *unimodal* case if the correlation is linear.

When plotting  $I_{150}$  versus  $I_{200}$  for all the regions (see Fig. 4), a general, well-defined relationship is observed. The relationship is similar to that for the associated LSB (values extracted from Table 2). A similar scatter in the correlation diagrams of the dust regions is observed. This consistency in the data for the different regions gives us confidence in the good quality of the data. At 90  $\mu\text{m}$  there is a trend similar to that of  $I_{150}$  versus  $I_{200}$ , however the correlation is less tight. Regions G6.5+36.5 and G187.4–16.7 appear to lie above the general trend. Finally, the  $I_{60}$  versus  $I_{200}$  correlation does not show a clear trend.

For wavelengths shorter than 150  $\mu\text{m}$ , correlations for regions such as G89.0–41.2 (the region in MBM55) and G301.2–16.5 (in Chamaeleon) are also unimodal. However, G187.4–16.7 (in L1563) and G301.7–16.6 exhibit a colour variation which is significantly better modelled by two linear ramps (case *bimodal*) with a wavelength-dependent turnover point. A significant flattening in the correlations is observed, indicating a decrease in the emission towards zones of high 200- $\mu\text{m}$  surface brightness. G111.2+19.6 and G297.3–15.7 cannot be classified due to a lack of short wavelength measurements.

The slopes for *unimodal* and *bimodal* cases of the different correlations are determined from a least-squares linear fit. For G297.3–15.7 we constrained the 200- $\mu\text{m}$  emission range up to 100  $\text{MJy sr}^{-1}$ . The regression fits are plotted in Fig. 3 and the resulting parameters (slopes, slope<sub>1</sub> and slope<sub>2</sub>, and offsets, offset<sub>1</sub> and offset<sub>2</sub>, for the first and second ramps, respectively) are given in Table 2. The errors in the slopes include the statistical uncertainties derived from the fits and the systematic uncertainties due to the actual responsivity variations.

The slopes (i.e. colour values) derived in this section are much more accurate than the absolute surface brightness values. Any flux offset, e.g. due to the ZL emission, dark current or zero-point error, has no effect on the determination of the slopes. In addition, the fitting procedure removes a considerable amount of the random noise of the individual pixels (due to, for example, cosmic glitches). Although the systematic calibration uncertainties, summarized in Section 3.1, may affect the colours, they act on the whole sample in the same direction. Thus, if we are interested mainly in *colour variations within the sample* then practically all systematic calibration uncertainties, related to, for example, improper knowledge of the effective solid angles per filter, are cancelled. In other words, even if our absolute colour values may be subject to some systematic calibration uncertainties, the internal ordering of the eight interstellar regions, e.g. by increasing the  $I_{150}/I_{200}$  ratio, is a very robust result. The only error factor affecting this internal ordering is the accuracy of the actual responsivity determination from the FCS data. Because the maps of different filter bands were taken at slightly different epochs, a responsivity variation between two maps may introduce an error in their ratio. In order to derive the corresponding uncertainty we determined the difference between the slope using the average of the two FCS measurements and the slope using only the second FCS measurement to compute the actual responsivities at each wavelength. The relative difference is always positive, with values between 3 and 9 per cent for the regions. Therefore, when

<sup>4</sup> Available at [ftp://nssdcftp.gsfc.nasa.gov/space-craft\\_data/cobe/dirbe/zsma/](ftp://nssdcftp.gsfc.nasa.gov/space-craft_data/cobe/dirbe/zsma/)

**Table 2.** The offsets and slopes in the regressions from ISOPHOT data and DIRBE predictions for ZL and LSB brightness corresponding to the dust regions. Systematic uncertainties due to the actual responsivity variations were added to the statistical uncertainties derived from the fits.

Name	$\lambda_{\text{ref}}$ ( $\mu\text{m}$ )	Offset <sub>1</sub> (MJy sr <sup>-1</sup> )	Slope <sub>1</sub>	Offset <sub>2</sub> (MJy sr <sup>-1</sup> )	Slope <sub>2</sub>	ZL (MJy sr <sup>-1</sup> )	LSB (MJy sr <sup>-1</sup> )
G6.5+36.5	60	11.1 ± 0.8	0.19 ± 0.04	–	–	11.9	1.7 ± 0.1
	90	4.2 ± 1.0	0.49 ± 0.09	–	–	6.6	7.5 ± 0.2
	150	4.0 ± 0.5	0.86 ± 0.04	–	–	2.5	21.1 ± 0.6
	200	0	1	0	1	1.3	21.7 ± 0.8
G89.0–41.2	60	5.2 ± 0.2	0.035 ± 0.007	–	–	9.7	0.89 ± 0.03
	90	5.1 ± 0.2	0.24 ± 0.04	–	–	5.3	2.8 ± 0.1
	150	5.3 ± 0.3	0.81 ± 0.07	–	–	2.0	6.2 ± 0.3
	200	0	1	0	1	1.0	5.7 ± 0.5
G90.7+38.0	60	3.4 ± 0.2	0.15 ± 0.03	–	–	3.7	0.57 ± 0.01
	100	2.3 ± 0.2	0.6 ± 0.1	–	–	1.6	1.71 ± 0.02
	150	0.3 ± 0.2	1.13 ± 0.05	–	–	0.7	3.56 ± 0.04
	200	0	1	0	1	0.4	3.72 ± 0.05
G111.2+19.6	150	3.4 ± 0.4	0.80 ± 0.02	–	–	0.9	17.8 ± 0.2
	200	0	1	0	1	0.4	19.3 ± 0.3
G187.4–16.7	60	1.6 ± 0.4	0.19 ± 0.02	9.0 ± 0.6	0.02 ± 0.02	12.9	2.73 ± 0.04
	80	3.3 ± 0.7	0.29 ± 0.04	18.7 ± 0.8	0.03 ± 0.04	9.3	6.84 ± 0.07
	90	3.0 ± 0.4	0.37 ± 0.06	19.0 ± 1.0	0.09 ± 0.06	7.3	11.14 ± 0.09
	100	6.0 ± 0.6	0.23 ± 0.04	19.0 ± 2.0	0.03 ± 0.05	7.5	14.6 ± 0.1
	120	6.4 ± 0.4	0.57 ± 0.01	19.0 ± 3.0	0.37 ± 0.04	4.7	22.0 ± 0.2
	200	0	1	0	1	1.4	30.8 ± 0.4
G297.3–15.7	150	11.9 ± 0.7	0.75 ± 0.02	–	–	0.9	25.0 ± 1.0
	200	0	1	0	1	0.5	27.0 ± 1.0
G301.2–16.5	60	5.1 ± 0.2	0.005 ± 0.003	–	–	4.7	1.93 ± 0.01
	90	8.8 ± 0.3	0.13 ± 0.02	–	–	2.5	6.28 ± 0.03
	120	9.8 ± 0.5	0.39 ± 0.01	–	–	1.6	12.35 ± 0.07
	150	5.1 ± 0.6	0.78 ± 0.02	–	–	0.9	17.2 ± 0.1
	200	0	1	0	1	0.47	17.8 ± 0.2
G301.7–16.6	60	3.6 ± 0.2	0.024 ± 0.007	4.7 ± 0.1	0.001 ± 0.004	4.7	1.93 ± 0.01
	90	5.1 ± 0.5	0.19 ± 0.03	11.1 ± 0.8	0.07 ± 0.03	2.5	6.28 ± 0.03
	120	6.0 ± 1.0	0.45 ± 0.04	13.0 ± 1.0	0.30 ± 0.04	1.6	12.35 ± 0.07
	150	7.4 ± 0.9	0.73 ± 0.06	–	–	0.9	17.2 ± 0.1
	200	0	1	0	1	0.5	17.8 ± 0.2

**Table 3.** Mean surface brightness,  $\langle I_{200} \rangle$ , and mean colour temperature,  $T$ , of the regions from ISOPHOT, mean surface brightness,  $\langle I_{200, \text{DIRBE}} \rangle$ , and mean temperature,  $T_{\text{DIRBE}}$ , obtained from DIRBE, and temperature of the LSB,  $T_{\text{LSB}}$ , from DIRBE. The ISOPHOT temperature errors include the statistical and systematic uncertainties.

Name	$\langle I_{200} \rangle$ (MJy sr <sup>-1</sup> )	$T$ (K)	$\langle I_{200, \text{DIRBE}} \rangle$ (MJy sr <sup>-1</sup> )	$T_{\text{DIRBE}}$ (K)	$T_{\text{LSB}}$ (K)
G6.5+36.5	30.2	15.6 ± 0.4	36.4	15.9 ± 0.2	17.0 ± 0.3
G89.0–41.2	22.2	15.1 ± 0.8	23.7	16.1 ± 0.2	18.4 ± 0.3
G90.7+38.0	6.2	18.9 ± 0.7	6.5	16.5 ± 0.3	16.8 ± 0.3
G111.2+19.6	30.0	15.0 ± 0.2	37.0	15.5 ± 0.2	16.4 ± 0.3
G187.4–16.7	46.9	–	36.0	–	–
G297.3–15.7	67.0 <sup>a</sup>	14.3 ± 0.2	–	14.7 ± 0.2	16.4 ± 0.3
G301.2–16.5	50.4	14.8 ± 0.2	30.7	16.1 ± 0.2	16.9 ± 0.3
G301.7–16.6	47.6	14.2 ± 0.6	29.4	15.9 ± 0.2	16.9 ± 0.3

Note. <sup>a</sup>This corresponds to the mean value for  $I_{200} < 100$  MJy sr<sup>-1</sup>.

computing the colour from two FIR maps measured with C200 in the same measurement sequence only these systematic uncertainties have to be added to the statistical errors (see  $I_{120}/I_{200}$ ,  $I_{150}/I_{200}$ ). Deriving colours from maps belonging to different detectors (e.g.  $I_{60}/I_{200}$ ) is a different issue because the actual responsivities of the two detectors are independent and not correlated. In order to

estimate the uncertainties in these situations, we used the values compiled in Table 3 from Schulz et al. (2002) from the dedicated photometric calibration source measurements.

We have plotted the slopes  $I_{\lambda}/I_{200}$  at 60 and 90  $\mu\text{m}$  versus  $I_{200}$  in Fig. 5. In the case of regions with *bimodal* behaviour, the two emission ratios are shown. These ratios decrease with the 200- $\mu\text{m}$

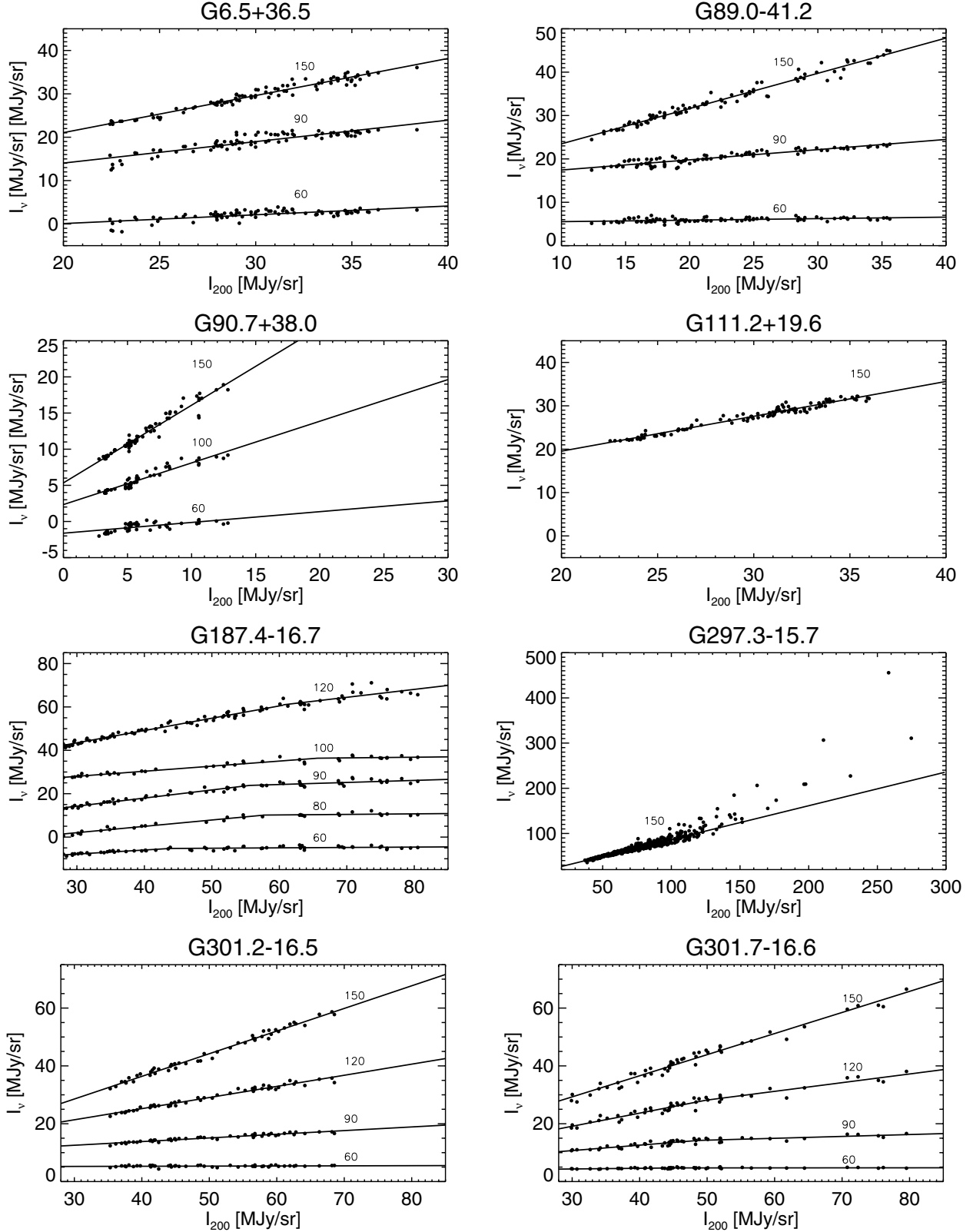


**Figure 3.** Surface brightness  $I_v$  versus  $I_{200}$  of the regions for wavelengths  $\lambda_{\text{ref}} = 60, 80, 90, 100$  and  $120 \mu\text{m}$ . Emission maps at  $60, 80, 90$  and  $100 \mu\text{m}$  were smoothed to the resolution of the  $200\text{-}\mu\text{m}$  scan. For a better view, maps were also shifted  $-15 \text{ MJy sr}^{-1}$  at  $\lambda = 60 \mu\text{m}$  for G6.5+36.5;  $-10 \text{ MJy sr}^{-1}$  at  $\lambda = 90$  and  $135 \mu\text{m}$  for G89.0-41.2  $-5$  and  $5 \text{ MJy sr}^{-1}$  at  $\lambda = 60$  and  $150 \mu\text{m}$ , respectively, for G90.7+38.0; and  $-15, -10, 15$  and  $20 \text{ MJy sr}^{-1}$  at  $\lambda = 60, 80, 100$  and  $120 \mu\text{m}$ , respectively, for G187.4-16.7.

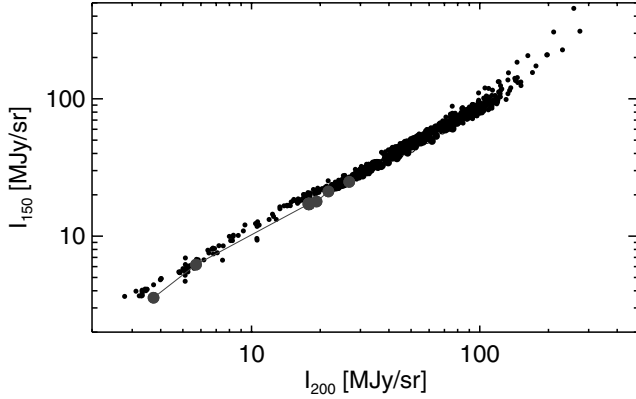


**Figure 4.** Surface brightness at 150  $\mu\text{m}$  versus surface brightness at 200  $\mu\text{m}$  (after subtraction of the ZL emission) in logarithmic scale for all regions. Large circles (connected by a solid line) correspond to the LSB emission derived from DIRBE data.

emission. In the  $I_{60}/I_{200}$  plot, we observe three regions (G90.7+38.0, G6.5+36.5, G187.4–16.7) with significant high  $I_{60}/I_{200}$  ( $>0.12$ ) at low  $I_{200}$  ( $<45 \text{ MJy sr}^{-1}$ ).

#### 4.2 Colour temperature from correlation $I_{150}$ – $I_{200}$

For each region, we have computed a colour temperature ( $T$ ) from the corresponding colour-corrected slope of correlation  $I_{150}$ – $I_{200}$  assuming that its spectral energy distribution (SED) is well represented by a modified blackbody  $F_\nu \propto \nu^\beta B_\nu(T)$ , where  $B_\nu(T)$  is the Planck function,  $\nu$  is the frequency, and  $\beta$  ( $\approx 2$ ) is the dust emissivity power-law index. Table 3 lists the colour temperature of each region, its mean surface brightness at (200  $\mu\text{m}$  ( $I_{200}$ )), the predicted DIRBE surface brightness at 200  $\mu\text{m}$  of the region ( $\langle I_{200, \text{DIRBE}} \rangle$ ), and the temperatures  $T_{\text{DIRBE}}$  and  $T_{\text{LSB}}$ , corresponding respectively to the region to and its LSB, derived from their predicted surface brightness values at 150 and 200  $\mu\text{m}$  (see Table 2). Despite the large difference in the beam size of DIRBE (40 arcmin) and ISOPHOT, the DIRBE predictions are good estimations because the variations in the physical conditions of the backgrounds are expected to be smaller than those among the regions, where the higher angular resolution of ISOPHOT is required to resolve them. Note that the dif-

ferences in surface brightness between ISOPHOT and DIRBE are relatively larger for regions G301.2–16.5 and G301.7–16.6 (see Table 3), with small sampled areas with ISOPHOT (see Table 1).

The relative differences between our colour temperatures and those derived from DIRBE are not larger than 13 per cent (see Table 3). These differences are partly due to angular resolution differences, and because of using different filter bands (100 and 240  $\mu\text{m}$  for DIRBE).

#### 4.3 Far-infrared extinction and grain opacity

The extinction obtained from star counts on the blue DSS plates has been correlated with the data at 200  $\mu\text{m}$ .

The ratios  $I_{200}/A_V$  for each region were determined from the pixel–pixel correlations  $I_{200}$  versus  $A_V$  by applying a least-squares fitting procedure. We used  $I_{200}$  as an ordinary variable and  $A_V$  as a random variable because the extinction data present a much lower signal-to-noise ratio. In other words, the random error in  $A_V$  is the main factor that produces the point scatter in the  $I_{200}$  versus  $A_V$  diagram. The statistical error in  $A_V$  was computed from the procedure described in Dickman (1978). This uncertainty, similar in all the fields ( $\pm 0.3 \text{ mag}$ ), was used to determine the output parameters of the fitting routine. As examples, Fig. 6 shows  $I_{200}$  versus  $A_V$  for G301.7–16.6 (top) and G187.4–16.7 (bottom). The resulting slopes ( $I_{200}/A_V$ ) and the Pearson correlation coefficients for all the regions are included in Table 4. The uncertainties in  $I_{200}/A_V$  correspond to  $1\sigma$  errors. The possible variation in  $R_V$  introduces a systematic uncertainty in  $A_V$  (see Section 3.2) and, therefore, in the ratio  $I_{200}/A_V$ , which can be up to 10 per cent reduced.

We also obtained the FIR grain opacity at 200  $\mu\text{m}$  ( $\tau_{200}$ ) normalized to  $A_V$  from the equation  $\tau_{200}/A_V = I_{200}/A_V / B_\nu(T)$ , using the inferred colour temperature ( $\beta = 2$ , cf. Table 3) and  $I_{200}/A_V$  (see Table 4).

### 5 INTERPRETATION

#### 5.1 Properties of the big grains

The emission in the two FIR bands, at 150 and 200  $\mu\text{m}$ , can be used to analyse the properties of the big grains in the regions. Our observations in Section 4.1 show that the correlation between  $I_{150}$  and  $I_{200}$

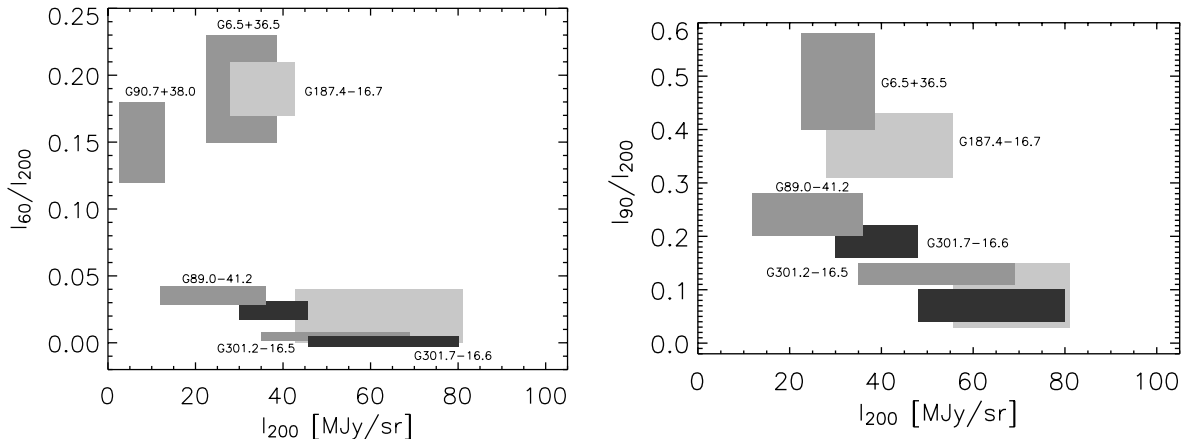


**Figure 5.** Colour-corrected ratios  $I_{60}/I_{200}$  and  $I_{90}/I_{200}$  (rectangles), as derived from the slopes of correlations  $I_{60}$  and  $I_{90}$  versus  $I_{200}$ . The width and height of the rectangles correspond to the 200- $\mu\text{m}$  surface brightness covered by the region and the statistical uncertainty, respectively. The black and light grey rectangles correspond to the bimodal cases G301.7–16.6 and G187.4–16.7, respectively; the rest of rectangles (dark grey) are unimodal cases. Lower limits of the rectangles in the 200- $\mu\text{m}$  emission axis are limited by the area sampled of each region (see Table 1).

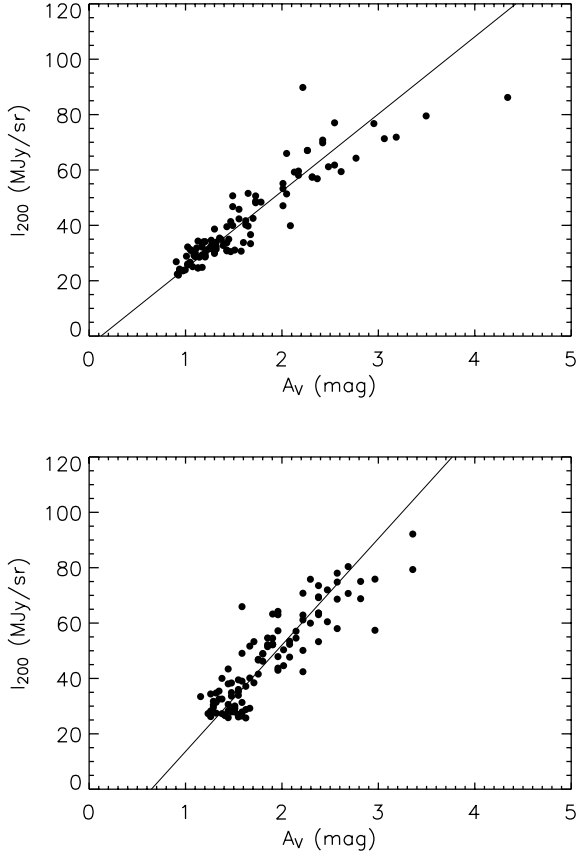


**Figure 6.**  $I_{200}$  versus  $A_V$  for the regions G301.7–16.6 (top) and G187.4–16.7 (bottom). The straight lines from the applied least-squares fitting procedure are also shown.

**Table 4.** The FIR dust 200- $\mu$ m emission and opacity normalized to visual extinction. Values of the Pearson correlation coefficient (PCC) for the  $I_{200}$ – $A_V$  correlation are also shown.

Name	$I_{200}/A_V$ (MJy sr <sup>-1</sup> mag <sup>-1</sup> )	PCC	$\tau_{200}/A_V$ (10 <sup>-4</sup> mag <sup>-1</sup> )
G6.5+36.5	26 ± 5	0.49	5 ± 1
G89.0–41.2	25 ± 3	0.61	6 ± 2
G90.7+38.0	22 ± 7	0.31	2.0 ± 0.8
G111.2+19.6	32 ± 7	0.48	8 ± 2
G187.4+16.7	38 ± 3	0.88	–
G297.3–15.7	21.1 ± 0.3	0.83	6.5 ± 0.5
G301.2–16.5	39 ± 3	0.59	10 ± 1
G301.7–16.6	28 ± 1	0.92	10 ± 2
DISM	21.1	–	2.4

is linear for each region, with no indication that the ratio  $I_{150}/I_{200}$  flattens within a region. As a consequence in all regions we find constant colour temperatures. These temperatures show a gradual variation as a function of the mean surface brightness of the region at 200  $\mu$ m (see Fig. 7). Only the region G90.7+38.0 shows a colour temperature in the range of the *diffuse* component identified from the Far-Infrared Absolute Spectrophotometer (FIRAS) and DIRBE data (Lagache et al. 1998). The rest of regions are within the temperature range of the so-called *dense* component (see Fig. 7). The smooth variation among the regions in the sample excludes the possibility that the emission of a region (above a constant background) comes

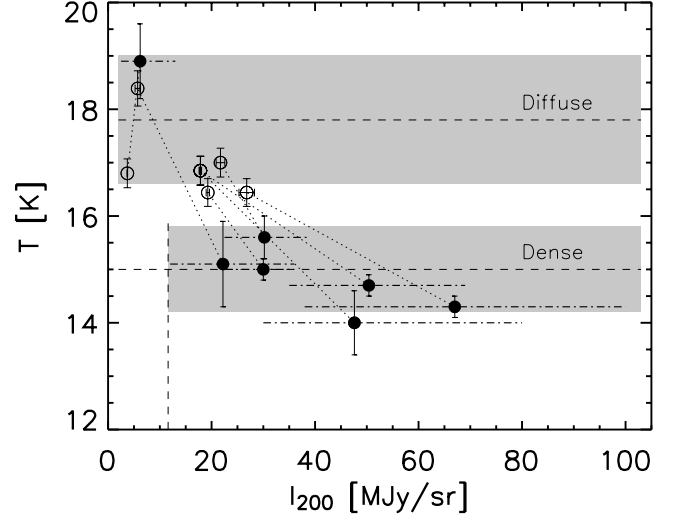


**Figure 7.** Colour temperatures corresponding to the dust regions (filled circles) and to the associated LSBs (unfilled circles) versus mean 200- $\mu$ m emission of the region. Systematic uncertainties can introduce a bias ( $\sim 10$  per cent) in the temperatures for all regions. Dotted lines link both temperatures for each region. Dot-dashed lines indicate the 200- $\mu$ m emission range for each region. Mean temperatures for the dense (dotted line) and diffuse components (dashed line) and respective dispersions (shadowed boxes) obtained from FIRAS and DIRBE (Lagache et al. 1998) are also shown. The vertical dashed axis marks the 200- $\mu$ m emission corresponding to the minimum column density for the existence of a dense component.

from a superposition of unrelated diffuse clouds. Consequently, the mean colour temperature of a region depends systematically on the dust column density above the background.

In Fig. 8 we investigate the ratios  $I_{200}/A_V$  and  $\tau_{200}/A_V$  as functions of colour temperature. There is no indication that the 200- $\mu$ m emission drops with decreasing temperature. On the contrary, the ratios are systematically higher than the ratio derived for the DISM. The calculation of  $\tau_{200}$  depends on  $T$  [ $\tau_v = I_v/B(v, T)$ ], but the quantity  $\tau_{200}$  should not. The resulting values of  $\tau_{200}/A_V$  are listed in Table 4. These normalized opacities exhibit a *systematic increase* with decreasing temperature.

We infer that the emitting grains systematically change properties as a function of the colour temperature. The big grains emit at submm wavelengths, more than can be expected from the analysis of the extinction maps in the V band.

## 5.2 Two-component model

An all-sky analysis of the *COBE* data by Lagache et al. (1998) indicated the presence of a component with  $T \sim 15$  K associated with dense molecular clouds and another with 17.5 K associated with dust in the atomic DISM. Similarly, Cambr  sy et al. (2001) analysed the FIR dust emissivity in the Polaris flare obtained from *COBE* and optical extinction data. They found that the FIR spectral energy distribution can be interpreted by assuming emission from two dust components with discrete temperatures. The ratio  $\tau_{100}/A_V$  indicates that the infrared emissivity of the cold component is higher than the warm component by a factor of 4. Cambr  sy et al. (2001) attribute this increase in FIR emissivity to a change in the properties of the big grains. A similar result is reported by Stepnik et al. (2003).

Following Cambr  sy et al., we assume that the regions studied by us consist of two emission components with different dust temperatures. The two emission components are both due to big grains. The



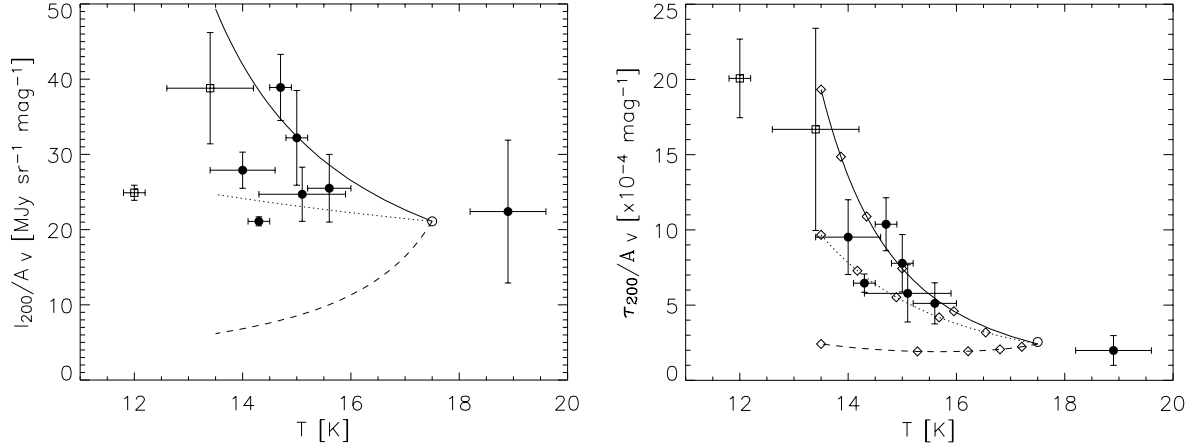


**Figure 8.** Left: the 200- $\mu$ m surface brightness normalized to  $A_V$  as a function of dust temperature. Right: the derived opacity  $\tau_{200}$  as a function of  $T$ . Dots correspond to the observed regions with ISOPHOT; squares to the PRONAOS observations of Polaris flare (Cambr  sy et al. 2001) and a dense filament in Taurus (Stepnik et al. 2003); the unfilled circle corresponds to the DISM, at 17.5 K. Dashed, dotted and solid lines correspond to models with  $\epsilon = 1, 4$  and 8, respectively.

FIR emission integrated along the line of sight has been modelled by changing the relative amounts of the components along the line of sight. For the warm component we adopt a dust temperature of  $T_w = 17.5$  K, similar to that of the DISM (Boulanger et al. 1996; Lagache et al. 1998). The temperature  $T_c$  for the cold component is assumed to be close to the lowest colour temperature measured in regions of medium column density ( $A_V < 6$  mag) representative of the sample in this paper. We choose  $T_c = 13.5$  K, the temperature of a medium density cloud in Ursa Major measured by Bernard et al. (1999). Consequently, the observed infrared emission can be written as

$$I_v = \tau_{v,c} B_v(T_c) + \tau_{v,w} B_v(T_w), \quad (1)$$

where  $\tau_{v,c}$  and  $\tau_{v,w}$  respectively give the infrared optical depths of the cold and warm components along the line of sight.

Apart from a temperature difference, the two dust components also differ in their infrared emission properties. The difference in dust emissivity between the cold and the warm components is characterized by  $\epsilon$  which gives the factor for which the emissivity of the cold component has been increased. In the case of Cambr  sy et al.,  $\epsilon = 4$ . Assuming that the optical extinction properties of the cold component are not substantially different from the warm component, we can write

$$\tau_{v,c} = \epsilon X \tau_{v,\text{tot}} \quad (2)$$

$$\tau_{v,w} = (1 - X) \tau_{v,\text{tot}}, \quad (3)$$

where  $\tau_{v,\text{tot}}$  is the total effective opacity in the case that the two components have identical infrared emission properties (i.e.  $\epsilon = 1$ ).  $X$  is the fraction ( $0 < X < 1$ ) of the opacity of the cold dust component with respect to the effective total opacity. Because we assume that  $\epsilon$  does not affect the optical extinction properties,  $\tau_{v,\text{tot}}$  is proportional to  $A_V$ . For both the warm and the cold dust components, we adopt a wavelength dependency  $\tau_v \propto \lambda^{-\beta}$  with  $\beta = 2$ .

We have computed the ratio  $I_{200}/A_V$  and a number of infrared colour ratios as a function of  $X$  for  $\epsilon = 1$  and  $\epsilon = 4$ . The results are presented in Fig. 9.

Fig. 9 shows that with  $\epsilon = 1$ , the ratio  $I_{200}/A_V$  drops significantly below the value of the DISM when increasing  $X$ . In addition, the variation of  $I_{200}/A_V$  is predicted to be very sensitive to  $X$ . On the

other hand, the surface brightness ratios are weak functions of  $X$  for  $X < 0.7$ , more closely resembling the colours of the warm component. Only for large amounts of cold dust  $X > 0.8$  the colour ratios are significantly affected. For the case  $\epsilon = 4$  (this value has been suggested by Cambr  sy et al. 2001 and Stepnik et al. 2003), the ratio  $I_{200}/A_V$  never drops below the value of the DISM. Already small amounts of cold dust ( $X \ll 1$ ) have a significant influence on  $I_{200}/A_V$  if compared with the case  $\epsilon = 1$ . The value of  $I_{200}/A_V$  exhibits a mild rise as a function of  $X$  and remains relatively close to the value of the DISM. The predicted surface brightness ratios in the case of  $\epsilon = 4$  decrease gradually as a function of  $X$ . Contrary to the case  $\epsilon = 1$ , the colour variation tends to flatten for  $X > 0.7$ .

For comparison with the observations we have determined the colour temperature  $T$  from  $I_{150}/I_{200}$ . The computed values of  $I_{200}/A_V$  and  $\tau_{200}/A_V$  as a function of  $T$  have been included in Fig. 8. We have added the case  $\epsilon = 8$  to illustrate the changes in  $\epsilon$ .

Direct evidence for  $\epsilon \gg 1$  is provided by the observed values of  $I_{200}/A_V$  which remain above that of the DISM. Our computations show that the ratio  $I_{200}/A_V$  must decrease when adding a colder dust component with  $\epsilon = 1$ . The addition of dust with an enhanced FIR emissivity  $\epsilon > 4$  causes  $I_{200}/A_V$  to remain above the value of the DISM for all  $X$ . Comparison of the model calculations with the observations (Fig. 10) strongly suggests that even high values of  $\epsilon$  ( $> 4$ ) are not ruled out by the observations.

The two-temperature model exhibits the interesting property that for  $\epsilon \approx 1$  the ratio  $I_{150}/I_{200}$  resembles the colour of the warm component for a large range of  $X$  ( $0 < X < 0.7$ ), whereas for  $\epsilon > 4$  the colours are closer to the cold component for  $X > 0.5$ . For each observed region, the pixel-to-pixel correlation diagram shows no significant change in  $I_{150}/I_{200}$ . In addition, all  $I_{150}/I_{200}$  ratios correspond to colour temperatures a few Kelvin lower than the temperature of the DISM of  $T_w = 17.5$  K. The absence of temperatures in the 15.6–17.5 interval supports the notion that  $\epsilon$  must be much larger than unity. Among the different regions, the ratio  $I_{150}/I_{200}$  exhibits significant variations suggesting that the clouds have different values for  $X$ .

The observations of  $\tau_{\text{FIR}}/A_V$  in the Polaris flare by Cambr  sy et al. (2001) show a similar behaviour to that which we find in our sample of clouds (Fig. 11). All temperatures are lower than 15.5 K and there is a systematic increase of  $\tau_{\text{FIR}}/A_V$  towards lower temperatures. Note that the FIR emissivity of the warm component

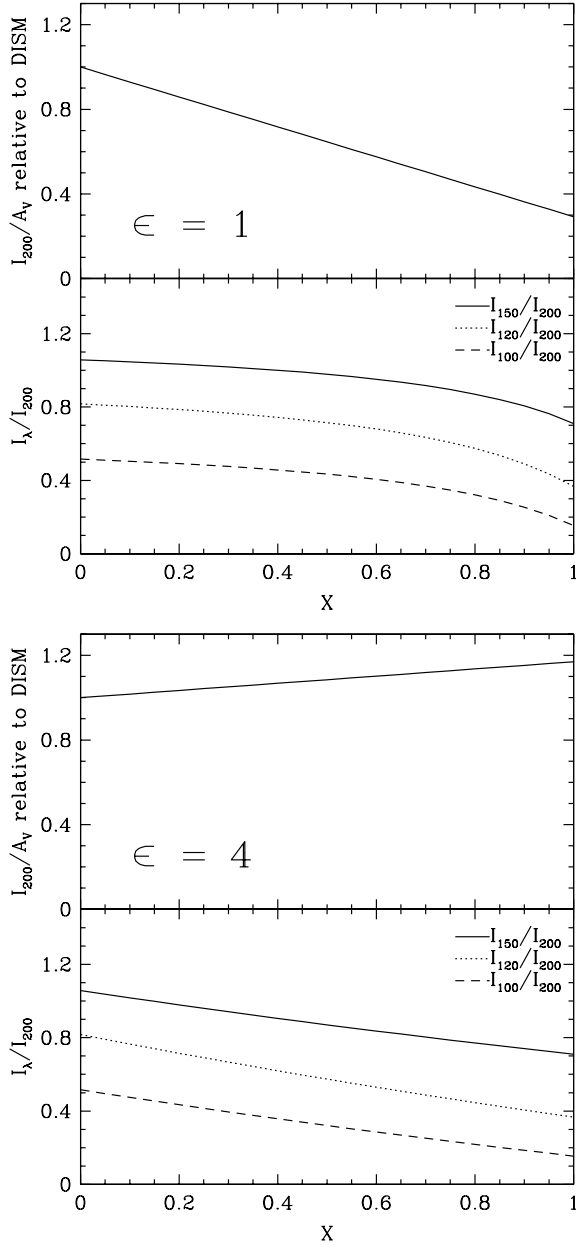


**Figure 9.** Calculations of infrared emissivity and colour ratios as a function of the cold dust fraction  $X$  assuming a warm and a cold dust component. We applied  $T_w = 17.5$  K and  $T_c = 13.5$  K. Top: the variation of the ratio  $I_{200}/A_V$  normalized to the value in the DISM and the ratios  $I_{150}/I_{200}$ ,  $I_{120}/I_{200}$  and  $I_{100}/I_{200}$  as a function of  $X$ . The dust of the cold temperature component has identical properties to the warm temperature component, i.e.  $\epsilon = 0$ . Bottom: similar to the upper panel, but with an enhanced emissivity for the cold dust component,  $\epsilon = 4$ .

in their work is 1.28 times higher than our value, therefore a factor of 4 emissivity enhancement found by them corresponds to a factor of 5 with our value of the DISM. Our model curve with  $\epsilon = 8$  shows an excellent match with the main distribution of  $\tau_{\text{FIR}}/A_V$  versus  $T$ . For the fraction of cold dust  $X$ , values ranging from 0.3 to 1 are predicted in the Polaris flare. Enhancements of about four times in the ratio  $\tau_{850}/\tau_V$ , from 20 to 12 K, have been found in the IC5146 molecular cloud filament from Submillimetre Common User Bolometer Array (SCUBA) observations at 450 and 850  $\mu\text{m}$  and near-infrared (NIR) imaging (Kramer et al. 2003).

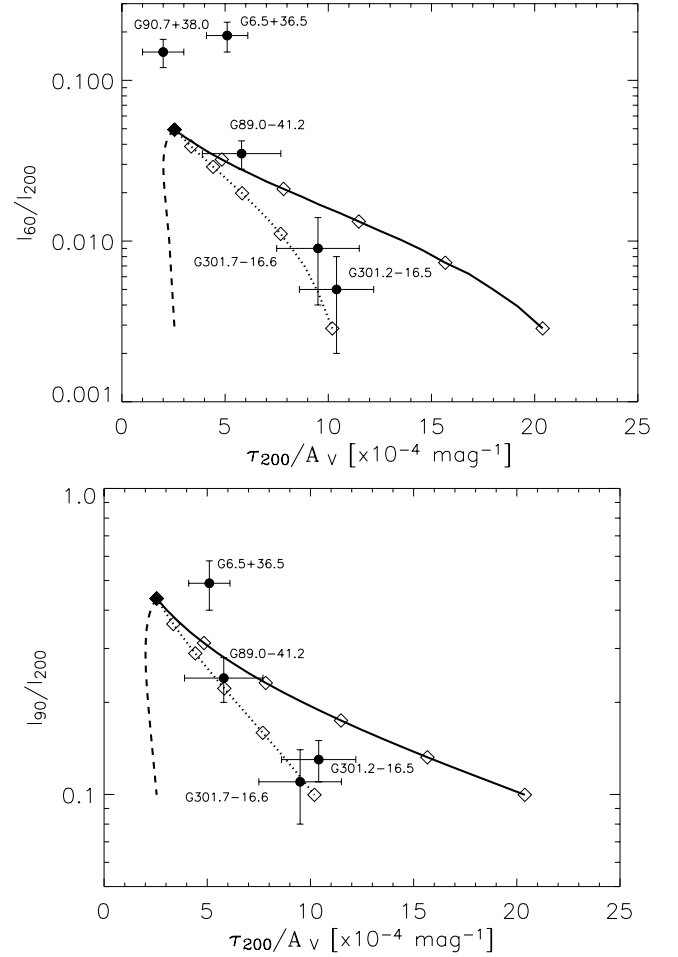


**Figure 10.** Ratios  $I_{60}/I_{200}$  (top) and  $I_{90}/I_{200}$  (bottom) versus  $\tau_{200}/A_V$  for the observed regions. Our two-component model predicted emission for the big grains (after inverse colour correction) for enhanced emissivities with  $\epsilon = 1, 4$  and  $8$ . Black and white (from left to right) diamonds correspond to a cold component fraction  $X = 0$  (DISM) and  $X = 0.2, 0.4, 0.6, 0.8$  and  $1$ , respectively. For the bimodal case G301.7–16.6 we have computed mean ratios (see Section 4.5).

### 5.3 Properties of the small grains

The  $I_{60}/I_{200}$  ratio is not constant but shows large variations among the regions suggesting a less homogeneous behaviour than the ratio  $I_{150}/I_{200}$  as a function of  $I_{200}$ . From Fig. 5 (left) we infer that the 60- $\mu\text{m}$  emission is higher in the low 200- $\mu\text{m}$  surface brightness regime. The excess at 90  $\mu\text{m}$  (Fig. 5, right) also decreases at larger 200- $\mu\text{m}$  emission. Note that for G301.7–16.6 the two ramps observed in correlation  $I_{90}$ – $I_{200}$  are for different emitting zones (low and high brightness correspond to the envelope and the core, respectively) and then we should avoid a direct comparison with the predicted value from  $I_{150}$ – $I_{200}$ , which corresponds to the complete dust region. The interpretation of the bimodal behaviour is out of the scope of our model (see Section 5.2). In the following we will use mean values for the ratios  $I_{60}/I_{200}$  and  $I_{90}/I_{200}$  of bimodal cases. These mean ratios are calculated from the two slopes weighted by the corresponding  $I_{200}$  dynamical range.

An infrared excess at 60 and 90  $\mu\text{m}$  with respect to the expected big grain emission indicates the presence of an additional emission component due to small grains. At a high 200- $\mu\text{m}$  surface brightness level, the 60- $\mu\text{m}$  emission shows a clear flattening (cf. the ratios)

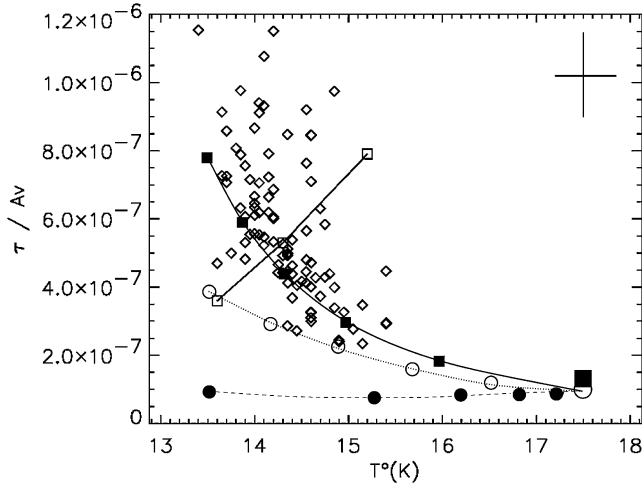


**Figure 11.** Here we show fig. 6 of Cambr  sy et al. (2001) (reprinted with permission of A&A) with the ratio between the opacity (normalized to  $1 \text{ cm}^{-1}$  assuming  $\beta = 2$ ) and the optical extinction versus temperature for the cold component in the Polaris flare (diamonds). The cross and unfilled squares indicate the typical statistical and systematic uncertainties, respectively. We have added the prediction from our model with enhancements of  $\epsilon = 1$  (filled circles),  $\epsilon = 4$  (unfilled circles) and  $\epsilon = 8$  (filled squares) for  $X = 0.2, 0.4, 0.6, 0.8$  and  $1$  (from right to left) using solid, dotted and dashed lines, respectively. The big filled square and the big circle correspond to the DISM ( $X = 0$ ) used by Cambr  sy et al. (2001) and by us, respectively.

suggesting that above a certain column density the small grain emission disappears. Regions that are situated on a high  $200\text{-}\mu\text{m}$  surface brightness pedestal are very likely embedded in an envelope with small grain emission. Fig. 10 supports this picture and links the depletion of the small grains with the observed enhanced emissivity of the big grains. We discuss this issue in the next section.

## 6 DISCUSSION

The separation of diffuse and dense regions as determined from the presence of  $60\text{-}\mu\text{m}$  emission (Lagache et al. 1998) can be understood in terms of the presence of a dust component with enhanced emissivity. Our model shows that the ‘cold’ regions can still contain large amounts of warm dust residing at the temperature of the DISM. The mixture of this warm component with a cold component with enhanced emissivity (along the line of sight) causes a quick drop in the FIR surface brightness ratios. The relative amount of this cold component can be small (i.e.  $X \ll 1$ ) as long as the emissivity enhancement is large ( $\epsilon > 4$ ). In the case where the cold component with enhanced emissivity is well mixed with the warm component, the drop in colour temperature between the true DISM dust and this mixture will be sharp even for small amounts of this cold component.

For two regions in the sample we find high ratios  $I_{60}/I_{200}$  but low FIR surface brightness ratios that correspond to apparent dust (colour) temperatures of less than  $16 \text{ K}$  (cf. Fig. 10 and Table 3). The region G6.5+36.5 is close to the dark nebula LDN134 where regions have been detected with a strong absence of  $60\text{-}\mu\text{m}$  emission (Laureijs et al. 1991). The region G187.4–16.7 exhibits a low ratio  $I_{120}/I_{200}$  corresponding to a colour temperature of  $15.4 \text{ K}$  in areas where the  $60\text{-}\mu\text{m}$  emission is prominent. This region covers LDN1563 where the centre of the cloud indicated by the peak  $I_{200}$  in Fig. 2 shows an absence of  $60\text{-}\mu\text{m}$  emission. These observations indicate that the presence of cold dust does not necessarily imply

a deficiency of  $60\text{-}\mu\text{m}$  emission along the same line of sight. On the other hand, the absence of  $60 \mu\text{m}$  does imply the presence of cold dust, as confirmed by the earlier studies on the  $60\text{-}\mu\text{m}$  deficient regions.

The change in emissivity for the cold big grain component is found to be large ( $\epsilon > 4$ ) and requires dramatic changes in general properties of the big grains. As discussed by Cambr  sy et al. (2001), the ratio  $\tau_{200}/A_V$  is proportional to the grain size. In addition, the buildup of porous composite grains through the process of coagulation can substantially increase  $\tau_{200}/A_V$  by a factor of at least 3 within the constraints set by the ultraviolet (UV) to NIR extinction curve. Although factors of  $\epsilon$  as high as 8 have to be confirmed by grain model calculations, an increase in emissivity several times larger than unity cannot be ruled out theoretically (see, for instance, Dwek 1997).

Variations in  $R_V$  from diffuse to dense clouds are interpreted due to changes in the optical properties of large dust grains in molecular clouds (Cardelli, Clayton & Mathis 1989). However, a possible increment of 10 per cent in  $A_V$  (see Section 4.3) cannot explain the observed high rise in  $\tau_{200}/A_V$  of the molecular regions with respect to the DISM.

Fig. 10 shows us that there is a correlation between the depletion of the emission at  $60$  and  $90 \mu\text{m}$  and the enhancement of the emissivity of the cold big grains. This result supports the coagulation process of the small grains on to big grains proposed by Stepnik et al. (2003). However, the amount of small grains required to form aggregations on the big grain surface is very large. A detailed study to explain the observed big grain emissivity enhancement could require a coagulation process in which big grains also aggregate to form dust grain aggregations.

In the analysis we used the ratios of  $I_{150}/I_{200}$  as representative of the low opacity parts of the clouds, as these regions make up for most of the data points in the correlation diagrams. We estimate  $A_V < 4 \text{ mag}$  at the ISOPHOT resolution because the dynamic range in  $I_{200}$  is less than  $50 \text{ MJy sr}^{-1}$  for all clouds in the sample except G297.3–15.7. We observe significant temperature variations among the regions in the sample. The observed temperatures range between  $14.1$  and  $15.6 \text{ K}$  cannot be explained with radiative transfer (cf. Stepnik et al. 2003). Therefore, it is more likely that the colour variations from cloud to cloud are predominantly due to a variation in  $X$ , as suggested by the model in Fig. 8.

For the higher density parts we do not rule out a drop in  $I_{150}/I_{200}$  similar to what has been observed for the other surface brightness ratios involving shorter wavelengths. For the regions covering very dense sightlines, a temperature drop due to radiative transfer effects together with a variation in  $X$  cannot be ruled out. However, these areas are expected to be small compared to the total area investigated.

## 7 CONCLUSIONS

All of the dust regions in our sample follow the same general, well-defined relationship  $I_{150}$  versus  $I_{200}$ , with a similar ‘pattern’ to that of the LSB. This suggests that both dusty environments have similar physical properties. The observed ratios  $I_{200}/A_V$  and  $\tau_{200}/A_V$  indicate an enhancement of the emissivity of the big grains (about four times) with respect to those in the DISM at low temperatures. We interpret this as a result of the presence of two components of big grains: a warm component ( $T \sim 17.5 \text{ K}$ ) and a cold component ( $T \sim 13.5 \text{ K}$ ) with an enhanced emissivity, whose mixing factor determines the colour temperature from  $150$  and  $200 \mu\text{m}$ . This cold big grain component is, therefore, always present and not only when

there is a depleted emission at 60  $\mu\text{m}$  as in the *PRONAOS* cases. The relationship  $I_{150}$  versus  $I_{200}$  is not linear, and its flattening towards higher surface brightness values (i.e. towards higher column density) is due to a major contribution from the cold component.

The small grains show a larger presence at low column densities, where we observe large variations of the emission excess at 60 and 90  $\mu\text{m}$  with respect to the emission at 200  $\mu\text{m}$ . The absence of 60- $\mu\text{m}$  emission does imply the presence of cold big grain dust. Conversely, the presence of cold big grain dust does not imply an emission deficit at 60  $\mu\text{m}$ .

The dependence of the small grain emission on the opacities normalized to the optical extinction of the big grains indicates a relationship between the physical properties of small and big grains. The small grains could be aggregating on the big grains in regions above a certain column density. The resulting big grains have different properties (emissivity and temperature) to those from the DISM.

## ACKNOWLEDGMENTS

This paper is based on observations with *ISO*, an ESA project with instruments funded by ESA member states (especially the PI countries France, Germany, the Netherlands and the United Kingdom) with the participation of ISAS and NASA.

CdB acknowledges support from the EC TMR Network POE. PÁ acknowledges support from the Bolyai fellowship and the Hungarian Research Fund (OTKA No. T037508). CdB and RJL acknowledge the hospitality of the Konkoly Observatory during their visit in 2001 August. The authors thank the anonymous referee for some comments which helped to improve this paper, and they also thank Neil Melville and Jody Kirchner for proofreading the manuscript.

The ISOPHOT interactive analysis (PIA) is a joint development by the ESA Astrophysics Division and the ISOPHOT Consortium; contributing ISOPHOT consortium institutes are DIAS, RAL, AIP, MPIK and MPA.

This research has made use of the USNOFS Image and Catalogue Archive operated by the United States Naval Observatory, Flagstaff Station (<http://www.nofs.navy.mil/data/fchpix>).

This publication makes use of data products from the Two Micron All Sky Survey, which is a joint project of the Univer-

sity of Massachusetts and the Infrared Processing and Analysis Center/California Institute of Technology, funded by the National Aeronautics and Space Administration and the National Science Foundation.

## REFERENCES

- Bernard J.-P., Boulanger F., Desert F. X., Puget J. L., 1992, *A&A*, 263, 258
- Bernard J.-P. et al., 1999, *A&A*, 347, 640
- Bok B. J., 1956, *AJ*, 61, 309
- Boulanger F., Falgarone E., Puget J. L., Helou G., 1990, *ApJ*, 364, 136
- Boulanger F., Abergel A., Bernard J.-P., Burton W. B., Desert F.-X., Hartmann D., Lagache G., Puget J.-L., 1996, *A&A*, 312, 256
- Cambr sy L., Boulanger F., Lagache G., Stepnik B., 2001, *A&A*, 375, 999
- Cardelli J. A., Clayton G. C., Mathis J. S., 1989, *ApJ*, 345, 245
- Desert F.-X., Boulanger F., Puget J. L., 1990, *A&A*, 237, 215
- Dickman R. L., 1978, *AJ*, 83, 363
- Dwek E., 1997, *ApJ*, 484, 779
- Gabriel C., Acosta-Pulido J., Heinrichsen I., Morris H., Tai W.-M., 1997, in Hunt G., Payne H. E., eds, *Proc. of the ADASS VI Conference*. Astron. Soc. Pac., San Francisco, p. 108
- Kelsall T. et al., 1998, *ApJ*, 508, 44
- Kessler M. F. et al., 1996, *A&A*, 315, L27
- Kessler M. F., M ller T. G., Arviset C., Garc a-Lario P., Prusti T., 2000, *The ISO Handbook Vol. I, ISO – Mission Overview, SAI-2000-035/Dc, Version.0*. ISO Data Centre, Villafranca del Castillo
- Kramer C., Richer J., Mookerjee B., Alves J., Lada C., 2003, *A&A*, 399, 1073
- Lagache G., Abergel A., Boulanger F., Puget J.-L., 1998, *A&A*, 333, 709
- Laureijs R. J., Mattila K., Schnur G., 1987, *A&A*, 184, 269
- Laureijs R. J., Clark F. O., Prusti T., 1991, *ApJ*, 372, 185
- Laureijs R. J., Klaas U., Richards P. J., Schulz B.,  br ham P., 2003, *ESA-SP/1262, The ISO Handbook Vol. IV, PHT – The Imaging Photopolarimeter*. ESA Publications Division, Noordwijk
- Lemke D. et al., 1996, *A&A*, 315, L64
- Lombardi M., Alves J., 2001, *A&A*, 377, 1023
- Mathis J. S., 1990, *ARA&A*, 28, 37
- Schulz B. et al., 2002, *A&A*, 381, 1110
- Stepnik B. et al., 2003, *A&A*, 398, 551

This paper has been typeset from a  $\text{\TeX}/\text{\LaTeX}$  file prepared by the author.